Full paper

Interplay between Aggregation and Coalescence: Experimental and Modeling Insights

S. Lazzari[1], B. Jaquet[2], L. Colonna[2], G. Storti[2], M. Lattuada[3], M. Morbidelli[2]*

[1]Department of Chemical Engineering, Massachusetts Institute of Technology, 77 Massachusetts Avenue, Cambridge, Massachusetts 02139, USA

[2]Institute for Chemical and Bioengineering, Department of Chemistry and Applied Biosciences, ETH Zurich, Vladimir-Prelog-Weg 1, 8093 Zurich, Switzerland

[3]Univ Fribourg, Adolphe Merkle Institute, Chemin des Verdiers 4, CH-1700 Fribourg, Switzerland.

*Corresponding author: massimo.morbidelli@chem.ethz.ch

A manuscript to be submitted to

Langmuir

Abstract

In the present work the aggregation behavior of polymeric particles possessing different glass transition temperatures (i.e. different "softness") has been studied in order to shed light on the interplay between aggregation and coalescence. In particular, the time evolution of the clusters hydrodynamic and gyration radii as well as of their structure factor has been monitored. With the help of an *ad hoc* developed deterministic model, based on population balance equations, it was possible to establish a link between the experimentally obtained light scattering data and the predicted particle size distribution. The simplicity of the model, involving one single adjustable parameter based on the coalescence characteristic time, allowed us to obtain a good accordance between simulations and experimental results with little computational effort.

Keywords:

Colloidal stability, Modeling, Hydrodynamic Radius, Gyration Radius, Light Scattering

1 Introduction

Various industrial processes rely on the handling of colloidal particles, may these be in the form of suspensions, emulsions or gels. As a matter of fact, colloidal particles applications range from food to plastics, going through paints, coatings, paper treatment, to more recent niche-fields, such as drug-delivery.[1]

One of the key features of colloidal particles is their kinetic stability, or the fact that the dispersed particle phase will sooner or later organize in larger structures (i.e. clusters) and phase-separate from the continuous phase it is suspended into. This un-avoidable process is regulated by the interplay of different phenomena occurring, such as aggregation and coalescence. Clearly

the environmental conditions (e.g. temperature, pH, shear rate) and the particles characteristics (e.g. surface charge, primary particle size), play a key role in determining the rate at which the destabilization process takes place.[2] Another feature of aggregating colloidal particles is their tendency to form self-similar (i.e. fractal) structures with fractal dimensions regulated by the conditions in which the destabilization occurs. The fractal dimension relates the aggregates mass x, with its size R:

$$x \propto R^{d_f} \tag{1}$$

For instance, rather open clusters are formed in fully destabilized systems where the cluster aggregation is diffusion limited (DLCA), whereas in reaction-limited cluster aggregation (RLCA) more compact clusters are formed, as not every aggregation event is an effective one due to typically charge-induced particles stability.[3] Note that when aggregation and coalescence occur simultaneously, the fractal dimension of the formed clusters is typically larger as compared to the non-coalescing cases. This is due to the fact that coalescence leads to an interpenetration of the particles constituting the cluster, therefore compacting the cluster itself and increasing its fractal dimension.

After the pioneering work by Ulrich and Subramanian,[4] highlighting how the simultaneous aggregation and coalescence was indeed shaping the soot cluster growth in flames, several authors dealt with this topic. Koch and Friedlander[5] introduced a simple, yet insightful and elegant deterministic model extending Smoluchowski's[6] approach to account also for coalescence. After that, Xiong and Pratsinis solved a 2-D population balance equation (PBE) based model accounting for the time-evolution of aerosol mass and surface area, and successfully compared it to experimental data.[7, 8]

Since then, during the last decades, the picture of aerosol coalescence and aggregation has become clearer as the characteristic times of metal particles has been quantified and the mechanism of coalescence unveiled.[9, 10] Moreover, the dynamics of cluster coalescence has been clarified and expressions describing the time-dependence of the fractal dimension proposed. While aerosols have been extensively investigated in this sense, only few studies are found on polymer particles undergoing aggregation and coalescence.[11, 12, 13, 14] These works helped clarifying how rubbery (i.e. fully coalescing) particles organize into clusters,[13] provided insights on the restructuring of preformed clusters undergoing coalescence upon temperature increase[14] and revealed a surface charge loss upon particle coalescence.[15] In these works particles were typically undergoing either full or no coalescence, hence existing light scattering correlations could be used to compare experimental results and PBE-based predictions. As a matter of fact the classical Smoluchowski approach used in these works provided good estimates of the experimental results using the fractal dimension (kept constant throughout the simulations) as the only fitting parameter. At the same time, such correlations cannot be employed for cases where the characteristic times of aggregation and coalescence are comparable, i.e. when partial coalescence occurs.

In this framework, the aim of this paper is to shed further light on the interplay between aggregation and coalescence along two main lines, namely i) developing a suitable 1-D PBE based model accounting for both processes and ii) correlating simulation results with light scattering results, thus extending the existing correlations for rigid clusters to partially coalesced ones. To this end, polymeric particles with different glass transition temperatures (T_g) have been prepared and their aggregation behavior studied in stagnant DLCA conditions. Different temperatures and particles concentrations have been explored in order to clarify the interplay of

the coalescence and aggregation rate. The developed model, along with the light scattering correlations, was tested against the experimental data to verify its reliability and potential.

2 Materials and methods

2.1 Materials

Butyl Acrylate (BA), Methyl methacrylate (MMA), Potassium Peroxydisulfate (KPS) and Sodium Chloride (NaCl) have been purchased from Sigma-Aldrich, sodium dodecyl sulfate (SDS) by Apollo Scientific. All chemicals had purities larger than 99% and were used as received. Millipore (MQ) water stripped for two hours with nitrogen was employed as the continuous phase in the emulsion polymerization. Ion-exchange resin (Dowex Marathon MR-3 hydrogen and hydroxide form) purchased from Sigma-Aldrich has been employed as received after the reaction to remove the SDS adsorbed on the particles surface.

2.2 Particles synthesis

The particles were synthesized by starved emulsion polymerization[16] employing the controlled reaction environment LABMAX©. In particular, the reaction was carried out at 70^{o}C in a 1 L jacketed reactor. The reactor was initially charged with stripped MQ water and SDS and heated up under nitrogen atmosphere. The initiator (KPS) solution was then added, and the monomer mixture feed was started. The conversion and particle size were followed by thermogravimetric analysis and dynamic light scattering (DLS), respectively. The instantaneous conversion always stayed above 99%, ensuring that starved conditions were achieved. The monomer feed was stopped when the particles reached the desired size. The reaction mixture was then kept at 70^{o}C during one hour, to ensure complete conversion of the monomer. After the

synthesis, the latexes were subjected to several cycles of cleaning using ion exchange resins until their surface tension was above 71 mN/m (Wilhelmy plate method).

2.3 Light Scattering

2.3.1 Dynamic Light Scattering

Dynamic light scattering was employed to monitor the particles size throughout the reaction (data not shown) until the desired particle diameter (200 nm) was reached. All the measurements were carried out using a BI-200SM goniometer system (Brookhaven Instruments, USA), equipped with a solid-state laser, Ventus LP532 (Laser Quantum, U.K.) of wavelength $\lambda_{DLS} = 532nm$, as the light source. The temperature was controlled by an external water bath with a precision of 0.1°C. The measurements were carried out in diluted conditions (occupied volume fraction $\phi = 1 \times 10^{-5}$) and with 10 mM NaCl.

2.3.2 Static Light Scattering

Static light scattering was employed to simultaneously follow the particle size (through the gyration radius $\langle R_g(t) \rangle$) and the fractal dimension evolution. The employed instrument was a Malvern Mastersizer 2000, equipped with a laser having $\lambda_{SALS} = 633nm$. The structure factor $\langle S(q,t) \rangle$ was obtained by dividing the measured scattered light intensity $\langle I(q,t) \rangle$ by the form factor $\langle P(q,t) \rangle$ of the primary particles, obtained by measuring the scattering intensity of the primary particles in non-aggregating conditions. The radius of gyration $\langle R_g(t) \rangle$ has been obtained by fitting the structure factor in a Guinier plot following the method described in Harshe et al.[17]

2.4 Differential Scanning Calorimetry

The glass transition temperatures of the samples were determined using a Waters Q200 differential scanning calorimeter. The samples were heated to 120 ^{o}C, cooled down to -50^{o}C and brought back to 120^{o}C. The heating rate was 10^{o}C/min in all cases.

3 Model development

3.1 Population balance equations

As previously discussed, two internal coordinates are in principle necessary to describe the time evolution of aggregating-coalescing systems, namely the cluster mass x (i.e. the number of primary particles in the cluster) and the fractal dimension d_f. The corresponding population balance equation is therefore two dimensional:[18]

$$\frac{\partial f\left(x,d_f,t\right)}{\partial t}+\underbrace{\frac{\partial}{\partial d_f}\left(f\left(x,d_f,t\right)v(x,d_f)\right)}_{A}=$$

$$\underbrace{-f\left(x,d_f,t\right)\int_0^{\infty}\int_1^3\beta(x,x_1,d_f,d_{f1})f\left(x_1,d_{f1},t\right)\mathrm{d}\,d_{f1}\,\mathrm{d}\,x_1}_{B} \tag{2}$$

$$\underbrace{+\frac{1}{2}\int_0^{\infty}\int_0^{\infty}\int_1^3\int_1^3\beta(x_1,x_2,d_{f1},d_{f2})f\left(x_1,d_{f1},t\right)f\left(x_2,d_{f2},t\right)\mu\,\mathrm{d}\,d_{f1}\,\mathrm{d}\,d_{f2}\,\mathrm{d}\,x_1\,\mathrm{d}\,x_2}_{C}$$

$$\mu=\delta_D\left(x-g_1(x_1,x_2)\right)\delta_D\left(y-g_2\left(x_1,x_2,d_{f1},d_{f2}\right)\right) \tag{3}$$

$$g_1\left(x_1,x_2\right)=x_1+x_2 \tag{4}$$

$$g_2\left(x_1,x_2,d_{f1},d_{f2}\right)=\frac{d_{fm}\ln\left(x_1+x_2\right)}{\ln\left(x_1^{\,d_{fm}/d_{f1}}+x_2^{\,d_{fm}/d_{f2}}\right)} \tag{5}$$

$$v\left(x,d_f\right)=\frac{1}{\tau_{COAL}\left(x\right)}\left(3-d_f\right) \tag{6}$$

$$\tau_{COAL}\left(x\right)=\tau_C x^{1/3}=\frac{\eta_p R_{p0}}{\sigma_p}x^{1/3} \tag{7}$$

The cluster mass distribution $f\left(x,d_f,\mathrm{t}\right)$ is defined such that $f\left(x,d_f,t\right)dxdd_f$ represents the concentration of clusters consisting of x to $x+dx$ primary particles having a fractal dimension comprised between d_f to d_f+dd_f at time t. Note that term A describes the variation in time of the rate of coalescence $v\left(x,d_f\right)$, and corresponds to a convective or Liouville term.[5] The rate of change of the fractal dimension is defined in equation (6) and depends on the coalescence characteristic time of the particles (cf. equation (7)) as detailed already by Koch and Friedlander.[5] Term B represents the loss of an x-sized cluster having fractal dimension d_f upon aggregation with any other cluster. Term C instead accounts for the formation of an x-sized cluster with fractal dimension d_f starting from two smaller aggregates which need to satisfy the two constitutive laws (equation (4) and (5)).[19] The integration boundaries are $\left[0;\infty\right)$ for the cluster mass and $\left[1;3\right]$ for the fractal dimension, accounting for all possible cluster masses and shapes. d_{fm} instead is the fractal dimension "imposed" by the aggregation regime, i.e. 1.7-1.8 in DLCA and 2.0-2.1 in RLCA conditions. σ_p,R_{p0},η_p represent the surface tension, radius and viscosity of a primary particle, respectively. $\beta\left(x_1,x_2,d_{f1},d_{f2}\right)$ instead is the aggregation kernel, which will be defined afterwards. All symbols are defined in the Symbol List in Appendix G of the Electronic Supporting Information (ESI).

Despite the solution of multidimensional balances is indeed possible,[18, 20] in this context a simplification of the balance to 1-D PBEs is desirable, as a fitting with experimental data has to be performed, requiring the iterative solution of the PBE. To reduce the problem to a 1-D PBE, it is necessary to multiply the original 2-D PBE (cf. equation (2)) with $\int_1^3 dd_f$ and $\int_1^3 d_f\, dd_f$, while introducing the following two distributions:

$$\omega(x,t) = \int_1^3 f\left(x, d_f, t\right) dd_f \tag{8}$$

$$\Omega(x,t) = \int_1^3 d_f f\left(x, d_f, t\right) dd_f \tag{9}$$

To properly treat the further terms present in the balance (2), the following assumption (cf. equation (10)) is made:

$$f\left(x, d_f, t\right) = \omega(x,t)\,\delta_D\left(d_f(t) - \overline{d_f}(x,t)\right) \tag{10}$$

where

$$\int_1^3 \delta_D\left(d_f - \overline{d_f}(x,t)\right) = 1 \tag{11}$$

The physical meaning of the latter assumption (10) is that the clusters of a given size x have the same fractal dimension $\overline{d_f}(x,t)$. The idea is to obtain two 1-D PBEs, the first one describing the cluster mass distribution (CMD) in time, while the second one describes their average fractal dimension evolution in time. As a difference to typically used models, the fractal dimension is time-dependent and a function of the (average) cluster size.

The resulting 1-D PBEs read:

$$\frac{d\omega(x,t)}{dt} = -\omega(x,t)\int_0^\infty \beta(x, x_1, t)\,\omega(x_1,t)\,dx_1 + \frac{1}{2}\int_0^x \omega(x - x_1, t)\,\omega(x_1,t)\,\beta(x - x_1, x_1, t)\,dx_1 \tag{12}$$

$$\frac{d\Omega(x,t)}{dt} - \frac{1}{\tau_{COAL}(x)}\omega(x,t)\left(3-\overline{d_f}(x,t)\right) = \\ -\Omega(x,t)\int_1^{\infty}\beta(x,x_1,t)\,\omega(x_1,t)\,dx_1 + \frac{1}{2}\overline{d_f}(x,t)\int_1^{x-1}\beta(x-x_1,x_1,t)\,\omega(x-x_1,t)\,\omega(x_1,t)\,dx_1 \tag{13}$$

where

$$\tau_{COAL}(x) = \tau_C x^{1/3} \tag{14}$$

$$\beta(x_1,x_2,t) = \frac{2}{3}\frac{k_B T}{\eta_c}\left(x_1^{1/\overline{d_f}(x_1,t)} + x_2^{1/\overline{d_f}(x_2,t)}\right)\left(x_1^{-1/\overline{d_f}(x_1,t)} + x_2^{-1/\overline{d_f}(x_2,t)}\right) \tag{15}$$

$$\overline{d_f}(x,t) = \frac{\Omega(x,t)}{\omega(x,t)} \tag{16}$$

The Liouville term vanishes in equation (12), as this balance accounts solely for the cluster concentration, disregardful of aggregates shape, whereas it is still present in equation (13); further details are reported in the work by Koch and Friedlander.[5] Note that $\beta(x_1,x_2,t)$ is the typical DLCA aggregation kernel, modified in order to account for a time-dependent fractal dimension. k_B is the Boltzmann constant, T the temperature and η_c the viscosity of the continuous phase.

Instead of solving the two PBEs (equation (12) and (13)) to calculate the average fractal dimension (equation (16)), it is possible to differentiate equation (16), obtaining an ODE system describing the time-evolution of the average fractal dimension (derivation details are reported in the ESI, Appendix A):

$$\frac{d}{dt}\left(\overline{d_f}(x,t)\right) = \frac{1}{\tau_C x^{1/3}}\left(3-\overline{d_f}\right) \\ \overline{d_f}(x,0) = 1.75 \quad \forall x \tag{17}$$

The initial condition selected, $\overline{d_f}(x,0)=1.75$, represents a typical fractal dimension of DLCA aggregating clusters.[2] It is hence sufficient to solve the PBEs (12) coupled with the ODE system (17): this way, one has directly the time evolution of the cluster concentrations while accounting for a time-dependent fractal dimension. Notably, equation (17) is actually analytically solvable and results in the following expression:

$$\overline{d_f}(x,t)=3-(3-1.75)\exp\left(-\frac{t}{\tau_C x^{1/3}}\right) \tag{18}$$

which is very similar to the one derived by Eggersdorfer et al., who studied the fractal dimension time-evolution of purely coalescing fractal clusters.[21]

To appreciate the features of equation (18), parametric simulations with different τ_C values for differently-sized clusters ($x=50,500,5000$) have been performed (cf. Figure 1).

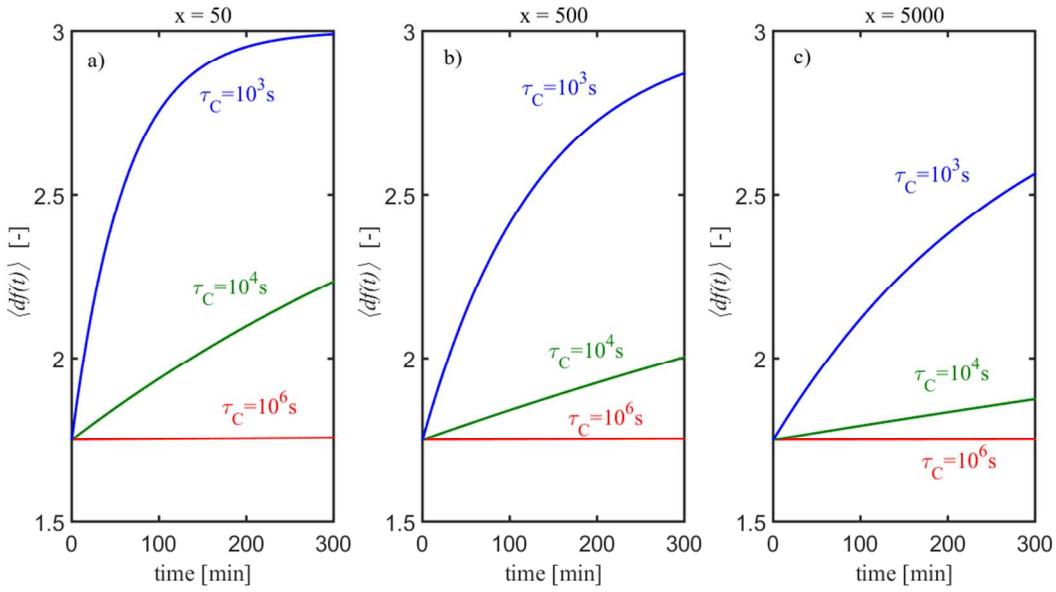

Figure 1

Fractal dimension vs time for differently sized clusters (x = 50, 500, 5000) and different τ_C.

A smaller τ_C implies a faster increase in the fractal dimension for a cluster of a given size as can be seen in Figure 1a), considering $\tau_C = 10^3 s$ (blue curve) and $\tau_C = 10^4 s$ (green curve). Comparing instead the time-evolution of the d_f of differently sized-clusters at the same τ_C it is observed how smaller clusters are able to re-arrange faster towards compact structures, exhibiting larger d_f (cf. Figure 1a) -1c) for $\tau_C = 10^4 s$). At the same time, if the τ_C is large enough as compared to the process time (τ_P) considered (e.g. $\tau_C = 10^6 s > \tau_P = 300\,\text{min} = 1.8\times10^4 s$), no coalescence is observed, no matter how small the cluster size considered (cf. Figure 1a)-1c) for $\tau_C = 10^6 s$).

3.2 Calculation of $\langle R_h(t)\rangle$, $\langle R_g(t)\rangle$ and $\langle S(q,t)\rangle$

Once in possession of the time-evolution of the cluster mass distribution, average properties, such as the hydrodynamic and gyration radii, $\langle R_h(t)\rangle$ and $\langle R_g(t)\rangle$, and the average structure factor $\langle S(q,t)\rangle$ have to be evaluated in order to compare them with experimental results obtained from light scattering. Such average quantities are defined as follows:

$$\langle R_h(t)\rangle = \frac{\int_0^\infty x^2\omega(x,t)S(x,q,t)\,dx}{\int_0^\infty \frac{x^2\omega(x,t)S(x,q,t)}{R_{h,eff}(x,t)}\,dx} \tag{19}$$

$$\langle R_g^2(t)\rangle = \frac{\int_0^\infty x^2\omega(x,t)R_g^2(x,t)\,dx}{\int_0^\infty x^2\omega(x,t)\,dx} \tag{20}$$

$$\langle S(q,t)\rangle = \frac{\int_0^\infty S(x,q,t)x^2\omega(x)\,dx}{\int_0^\infty x^2\omega(x)\,dx} \tag{21}$$

While the cluster distribution $\omega(x,t)$ is known once the PBEs have been solved (equation (12)), suitable expressions for the hydrodynamic and gyration radii of each cluster, i.e. $R_{h,eff}(x,t)$ and $R_g(x,t)$ as well as for the structure factor $S(x,q,t)$ are needed. q represents the scattering wave vector, defined as:

$$q = \frac{4\pi n}{\lambda}\sin\left(\frac{\theta}{2}\right) \tag{22}$$

where θ is the scattering angle, λ is laser wavelength and n is the refractive index of the continuous phase. Note that in the present case, clusters may aggregate and coalesce simultaneously and therefore the usually reported formulas to calculate $R_{h,eff}(x,t)$ and $R_g(x,t)$

in the case of rigid spheres cannot be employed.[22, 23] For the sake of brevity the full derivation of the average quantities $\langle R_g(t)\rangle$, $\langle R_h(t)\rangle$ and $\langle S(q,t)\rangle$, is reported in the ESI in Appendix B.

4 Numerical Solution

In the present simplified form, the balance on $\omega(x,t)$ would require a significant number of ordinary differential equations (ODE) to be solved, as the internal coordinate x can go up to roughly $10^4 - 10^5$ units. In order to reduce the problem size, a discretization method, based on Gaussian basis functions is employed.[18, 20, 24] The main advantage of the present method is the ease with which it allows to deal with the convolution integrals. The key idea is to approximate the actual distribution function with a sum of Gaussian basis functions:

$$\omega(x,t) \cong \sum_{i=1}^{N_G} \alpha_i(t)\, e^{-s_i(x-x_i)^2} \tag{23}$$

This allows to solve a finite number of ODEs (namely N_G) to obtain the time-dependent coefficients $\alpha_i(t)$, while the grid positions where the Gaussians are centered (x_i) are fixed before the integration start. The parameter s_i describes the overlapping degree of the Gaussians and is fixed once the Gaussian centers are defined:[20]

$$s_i = \frac{1}{(x_{i+1} - x_i)} \tag{24}$$

To obtain the discretized balances it is sufficient to plug in the approximations (23) in the PBE in (12). Further details are discussed in the ESI, Appendix C, whereas the final balance reads:

$$\underline{\underline{C}}\frac{d\underline{\alpha}}{dt} = -2\underline{\underline{C}}\underline{\alpha}\sum_{j=1}^{N}\alpha_j\sqrt{\frac{\pi}{s_j}} - \underline{\underline{C}}\underline{\alpha}^{W_2}\sum_{j=1}^{N}\alpha_j^{W_1}\sqrt{\frac{\pi}{s_j}} - \underline{\underline{C}}\underline{\alpha}^{W_1}\sum_{j=1}^{N}\alpha_j^{W_2}\sqrt{\frac{\pi}{s_j}} + \underline{\underline{\psi}}\underline{\gamma} + \underline{\underline{\psi}}\underline{\gamma}^{W} \tag{25}$$

The vectors and matrixes occurring in equation (25) are also defined in Appendix C.

5 Results and discussions

5.1. Particle characterization and experimental conditions

The different nanoparticles used in this study, prepared as described in Section 2, are presented in Table 1, where details about their composition, size, stability and glass transition temperature (T_g) are found.

Table 1 - Particle characterization

MMA [% wt]	BA [% wt]	Diameter [nm]	PDI [-]	CCC* [M NaCl]	T_g [^{o}C]
30	70	198	0.027	0.75	-12
50	50	202	0.016	0.65	17
60	40	199	0.017	0.75	36
70	30	198	0.021	0.25	54

*The critical coagulation concentration (CCC) is measured at 25^{o}C

Particles spanning through a quite large range of T_g (-12^{o}C to 54 C) were produced. Note that the reported T_g values represent an indication of the temperature interval at which the transition between a glassy and a rubbery polymer matrix is observed.

The aggregation behavior of the particle systems has been studied in fully destabilized DLCA conditions, achieved by diluting the latexes in 4 M NaCl water solutions. This specific salt concentration was chosen as it guaranteed a density match between the continuous phase and the particle phase, preventing cluster sedimentation to interfere with the experiments.

Aggregation experiments were performed at room temperature in static light scattering (SLS) experiments, whereas in a range between 25-45°C when using dynamic light scattering (DLS). The corresponding viscosities of the continuous phases (given the 4M NaCl concentration) are reported in Table D1 (ESI, Appendix D).[25]

5.2 Aggregation at room temperature: $\langle R_g(t)\rangle$, $\langle R_h(t)\rangle$ and $\langle S(q,t)\rangle$

Static light scattering (SLS) experiments were performed at 25°C and 4 M of NaCl. Both the average radius of gyration $\langle R_g(t)\rangle$, and the structure factor $\langle S(q,t)\rangle$ have been measured in time at three different occupied volume fractions, namely $\phi = 1\times10^{-5}, 2\times10^{-5}, 3\times10^{-5}$. In Figure 2a)-c) the measured $\langle R_g(t)\rangle$ vs. time is shown for all concentrations and particle types employed.

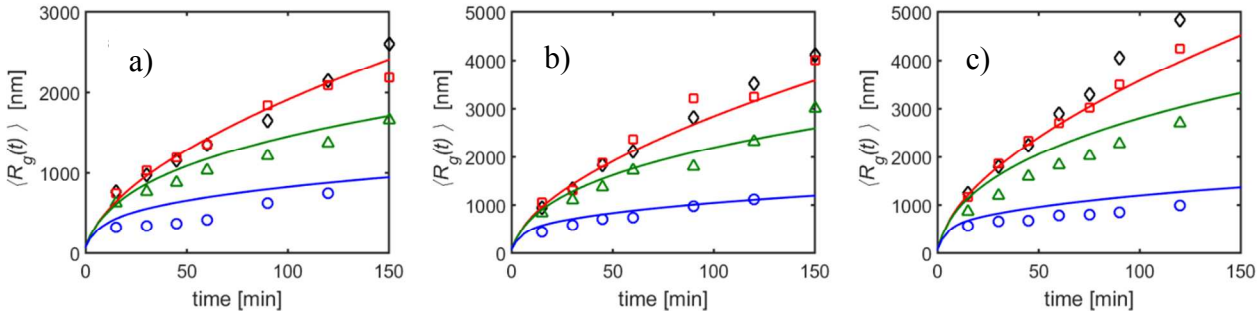

Figure 2

$\langle R_g(t)\rangle$ for the different particles at 25°C and a) $\phi = 1\times10^{-5}$, b) $\phi = 2\times10^{-5}$ and c) $\phi = 3\times10^{-5}$. Black diamonds: 70% MMA, red squares: 60% MMA, green triangles: 50%MMA, blue circles: 30% MMA particles, continuous lines: corresponding model predictions. Note that the $\langle R_g(t)\rangle$ predictions for the 70% and 60% MMA overlap. All the parameters values employed to obtain the model predictions are reported in Table D2 (ESI, Appendix D).

$\langle R_g(t)\rangle$ increases in time for all particle types, although the lower the T_g (i.e. the lower the MMA % and the softer the particles), the smaller is the $\langle R_g(t)\rangle$ observed, both in terms of absolute value and increase rate. This might seem surprising considering that the DLCA characteristic time of (doublet) aggregation (τ_A) is composition-independent:

$$\tau_A = \frac{1}{\beta_{11}^{DLCA} C_{part}} = \frac{3\eta_C}{8k_B T C_{part}} \tag{26}$$

As can be seen from equation (26), τ_A depends only on the temperature of the system (25°C in this set of experiments) and the viscosity of the continuous phase η_C (cf. Table D1, Appendix D, ESI) and it is defined for all systems once the particle number concentration C_{part} is fixed. The smaller $\langle R_g(t)\rangle$ observed for the softer particles (at a given particle concentration) can be rationalized as follows. When soft particles aggregate into clusters, neighboring particles (in the aggregate) will eventually coalesce with one another, leading to a more compact cluster with a smaller $\langle R_g(t)\rangle$ as compared to equally-sized aggregates consisting of rigid particles, which are typically more open. This structural difference affects also the aggregation rate: open clusters

have a larger collision radius than compact ones (of the same mass) and their aggregation probability is therefore larger. Thus, although τ_A is per definition composition-independent, the softness of the particles in an aggregate indirectly impacts the aggregation rate by affecting the cluster spatial organization. Deepening whether and to which extent particles in a cluster undergo coalescence, is therefore key.

A powerful and yet simple way to understand this is based on the comparison of the relevant characteristic times involved. Besides the already introduced characteristic time of doublet coalescence τ_C (cf. equation (7)) and of doublet aggregation τ_A (cf. equation (26)), also the characteristic time of the entire aggregation process (τ_P), defined as the total time for which the system is observed, plays an important role in this context. Notably, $\tau_P > \tau_A$ in all cases, otherwise no clusters would be formed if the process time was shorter than the characteristic time of doublet formation. To ease the analysis it is convenient to introduce the ratio N of the doublet coalescence and aggregation characteristic times:

$$N = \frac{\tau_C}{\tau_A} \tag{27}$$

It is now possible to distinguish three limiting cases:

i) $N \ll 1$ - as soon as the primary particles aggregate, they undergo instantaneous coalescence and the obtained clusters are fully compact all along the aggregation process.

ii) $N \approx 1$ - doublet aggregation and coalescence occur at a comparable time scale. Since the process time $\tau_P > \tau_A \approx \tau_C$ the clusters grow while coalescing, hence rather uniformly compact aggregates are formed. Such uniformity should be granted even though clusters born at different times exhibit different coalescence extents, as the clustering process is

mediated by cluster-cluster aggregation, which averages out possible local non-homogeneities.

iii) N >>1 - in this latter case, two further sub-cases have to be distinguished:

a) $\tau_P < \tau_C$ - no coalescence occurs as this process is too slow (it lasts even longer than the full aggregation process); open clusters are formed.

b) $\tau_P > \tau_C$ - coalescence occurs slowly and only after the clusters are formed. The aggregate "history" or "life" becomes relevant: neighboring particles in a cluster formed at the beginning of the aggregation process will exhibit a larger degree of coalescence as compared to particles which only "recently" became neighbors. On average, the clusters will exhibit (according to the absolute values of τ_P and τ_C) a rather open structure with coalesced braches. As compared to case ii) a smaller degree of compactness (i.e a smaller d_f) is expected to be found, unless $\tau_P \to \infty$.

Being based on the τ_A and τ_C of doublets, the latter picture is a simplistic one, nevertheless representing an insightful view into the aggregation-coalescence process.

When fitting the model predictions against the experimental data using as only fitting parameter τ_C, one obtains the following results: $\tau_C \to \infty$ (i.e. $\tau_C > 10^8 s$) for the 70% and 60% MMA particles, $\tau_C \approx 4300 s$ for the 50% MMA case and $\tau_C \approx 100 s$ for the 30% MMA particles. The simulated $\langle R_g(t) \rangle$ are reported in Figure 2 a)-c) (continuous lines) for the different particle concentrations; the good agreement with the experimental data shows the model capability to capture the underlying physics of the model. Given such τ_C values, it is possible to compare

them with $\tau_P \approx 150\,\text{min} = 9000s$ and τ_A (cf. Table 2) along the previously described three limiting cases i)-iii).

Table 2 τ_A at 25°C and 45°C, for the different particle systems

$\phi\,[-]$	$\tau_A\,[s]$ at 25°C	$\tau_A\,[s]$ at 45°C
1 x 10^{-5}	48	31
2 x 10^{-5}	24	15
3 x 10^{-5}	16	10

It is clear that being $\tau_C \to \infty$ for the 60% and 70% MMA cases, these two types of particles will never undergo coalescence (cf. case iii a)) given that $\tau_C >> \tau_A$ ($N >> 1$) and $\tau_C >> \tau_P$. Note that the predictions of $\langle R_g(t) \rangle$ for these two cases are superimposed and represent a typical DLCA case of non-coalescing particles (cf. Figure 2a)-c)). Such a behavior is consistent with the T_g of these particles systems, which is larger (36°C and 54°C for the 60% and 70% MMA, respectively) than the experimental one (25°C), thus coalescence is not expected to occur. The 50 % MMA containing particles instead belong to case iii b) because while $\tau_C > \tau_A$ $(N > 1)$ for any ϕ , $\tau_P > \tau_C$, allowing the formed clusters to undergo partial coalescence. This observation is supported by the T_g of the 50% MMA particles, which is slightly lower than the experimental one (17°C vs 25°C), thus allowing partial coalescence to occur. The 30% MMA case on the other hand falls in case ii) as $\tau_C \approx \tau_A$ $(N \approx 1)$; being the values very close, a significant extent of coalescence, much larger than the one of the 50% MMA particles, is expected to occur,

especially considering the long process time $\left(\tau_P > \tau_A \approx \tau_C\right)$ and the significant difference in terms of T_g vs T (-12°C vs 25°C).

To further explore the model potential, the predictions of the hydrodynamic radius $\left\langle R_h(t)\right\rangle$ (according to equation (19)) of the 60%, 50% and 30% MMA containing particles have been compared with the corresponding DLS experimental results at 25°C and $\phi = 1\times10^{-5}$ in Figure 3.

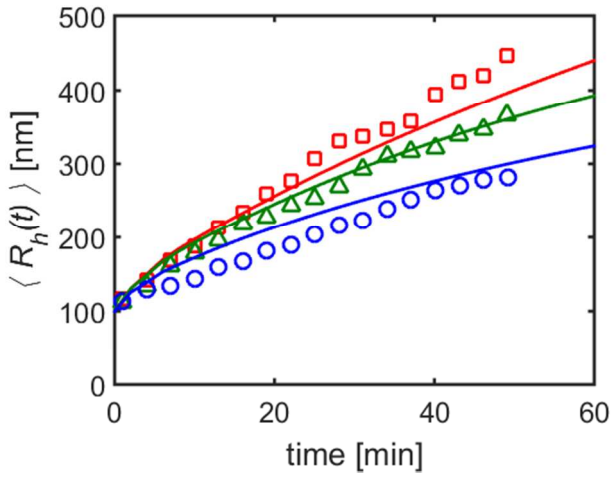

Figure 3 $\left\langle R_h(t)\right\rangle$ of the 60% MMA particles (red squares), the 50% MMA particles (green triangles) and the 30% MMA particles (blue circles) and their corresponding simulations (continuous lines) All the parameters employed to obtain the model predictions are reported in Table D2 (ESI, Appendix D).

Note that the τ_C values employed in these simulations were the ones obtained from the fitting of the $\left\langle R_g(t)\right\rangle$ data, hence the simulated curves in Figure 3 are purely predictive. The reasonable agreement between simulations and experiments evidences the model reliability and its capability to capturing the complex physics of the aggregating-coalescing system. When

particles are significantly (if not almost completely) coalescing (30% MMA case), a limited overestimation of the model prediction is observed for both $\langle R_g(t) \rangle$ and $\langle R_h(t) \rangle$. This is probably due to the fact that the equations derived for the calculation of $\langle R_g(t) \rangle$ and $\langle R_h(t) \rangle$ have been obtained for the intermediate situation of partially coalescing particles and not for full coalescing systems.

Having explored the model effectiveness in describing size averages, it is now desirable to test its performance in terms of cluster-structure related quantities and to deepen the interplay between aggregation and coalescence in determining the clusters spatial organization. As a first step, the average number of particles constituting the clusters (i.e. the cluster mass), $N_{AVE}(t)$, defined as:

$$N_{AVE}(t) = \frac{\int_0^\infty x\omega(x,t)\,dx}{\int_0^\infty \omega(x,t)\,dx} \tag{28}$$

is calculated at 25°C at $\phi = 1\times10^{-5}, 2\times10^{-5}, 3\times10^{-5}$ for the 60%, 50% and 30% MMA containing particles, employing the previously fitted values of τ_C. The simulation results are reported in Figure 4.

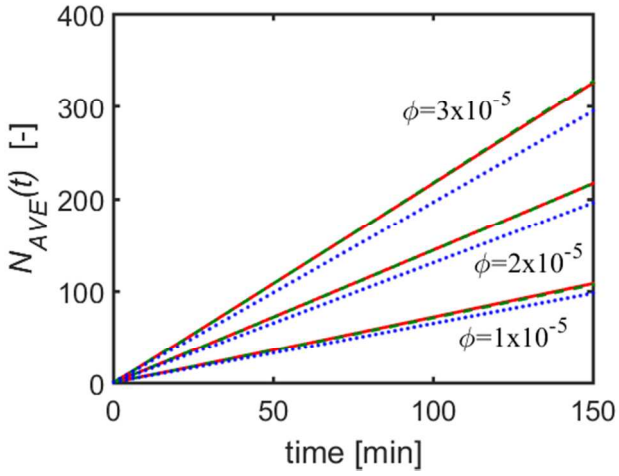

Figure 4 - $N_{AVE}(t)$ at 25°C for $\phi = 1\times10^{-5}, 2\times10^{-5}, 3\times10^{-5}$. Red continuous lines: 60% MMA; Green dashed lines: 50% MMA particles (almost overlapped with the 60% MMA), dotted blue lines: 30% MMA particles. All the model parameters values employed to obtain the model predictions are reported in Table D2 (ESI, Appendix D).

As can be seen from Figure 4, the average mass of the clusters is smaller for aggregates consisting of soft particles. This is due to the decreased reactivity of soft clusters as a result of their higher compactness and reduced collision radius. Notably though, the observed differences in N_{AVE} (for one set of ϕ) among the different types of particles are relatively small: in the considered time-interval the largest relative difference between cluster masses is of about 10% (comparing the 30% MMA and the 60% MMA particles). In other words, the difference in reactivity induced by the different softness is present, but only mildly affects the average cluster mass. From the $\langle R_g(t) \rangle$ trends (cf. Figure 2) on the other hand, where the soft 30% MMA particles were showing much smaller radii (by at least 100%) when compared to the 60% MMA particles, the significant impact of the particle softness on the clusters morphology can be

appreciated. More explicitly, the softness of the aggregating particles strongly affects the spatial organization of the resulting clusters but only mildly impacts the overall aggregation kinetics.

Having qualitatively discussed the impact of coalescence on the aggregates structure, it is now interesting to attempt a more quantitative description. For this reason, the SLS experimental data on the average structure factor $\langle S(q,t)\rangle$ (obtained at 25°C, 4 M NaCl and three different occupied volume fractions, $\phi = 1\times10^{-5}, 2\times10^{-5}, 3\times10^{-5}$) have been compared with the corresponding predicted $\langle S(q,t)\rangle$ (cf. equation(21)) at three different time points, namely 60, 90 and 120 minutes. Note that the model is employed here in "prediction mode", as the employed τ_C values in the different cases are those previously fitted against the $\langle R_g(t)\rangle$ data set. The results of the comparison are shown in Figure 5.

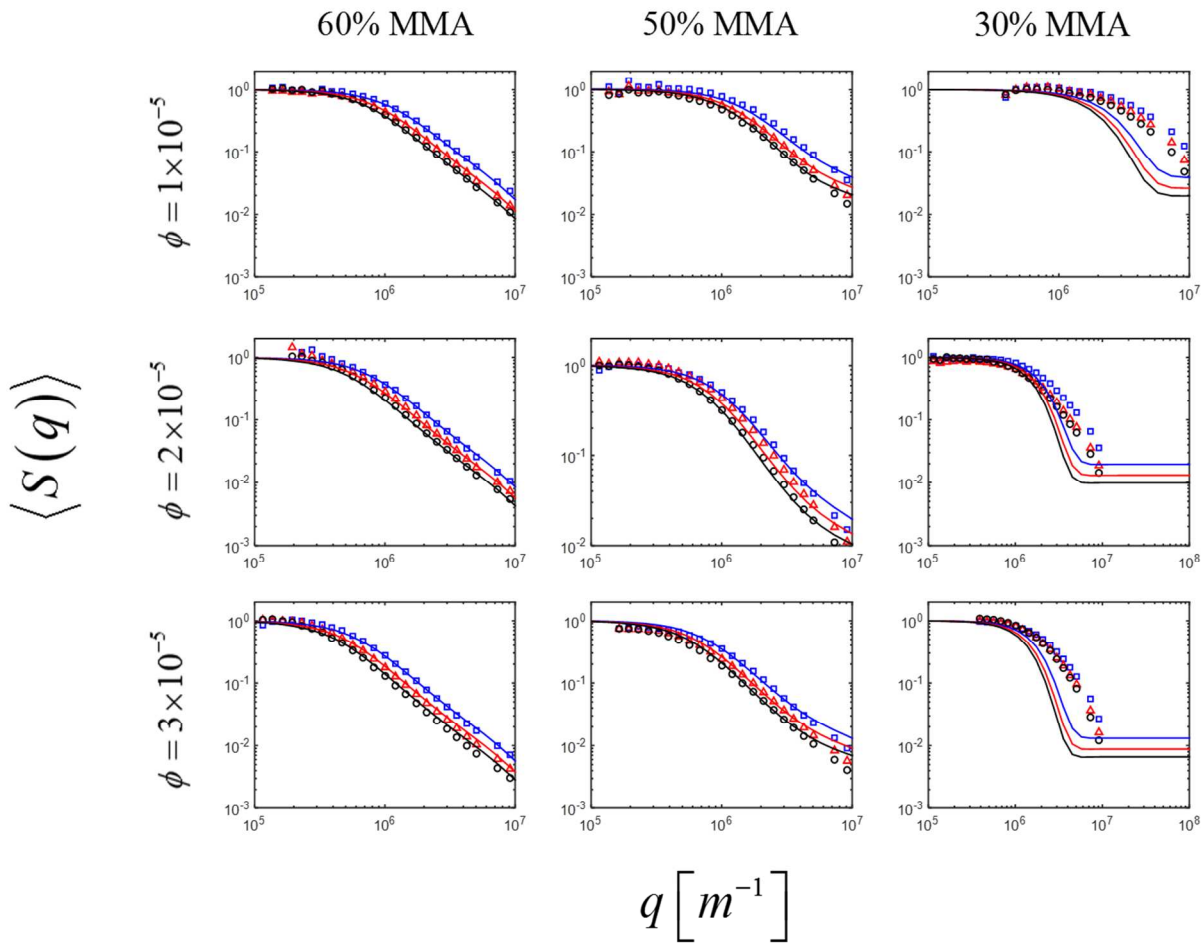

Figure 5 – Experimental (symbols) and predicted (continuous lines) $\langle S(q,t)\rangle$ at three different times: 60 min (blue squares), 90 min (red triangles), and 120 min (black circles). All the parameters employed to obtain the model predictions are reported in Table D2 (ESI, Appendix D).

From Figure 5 it can be seen that the predictions of the model well-describe the experimental observation in the cases of 60% and 50% MMA containing particles, whereas a poor agreement is found in the 30 % MMA case. This implies that the model is indeed suitable for describing not only average sizes, but gives also meaningful insights regarding the structure of clusters undergoing simultaneous aggregation and coalescence. This holds provided that there is no or

only partial coalescence: when approaching full coalescence the model offers only a qualitative description. As a matter of fact, for the 30% MMA case, the slope of $\langle S(q,t)\rangle$ vs. q (which represents the $\langle d_f(t)\rangle$ of the clusters)[2] increases in time, suggesting that cluster coalescence is significantly occurring. To further prove this point, the scattered intensity for the 30% MMA clusters has been recalculated assuming fully coalesced clusters (i.e. spheres) using the Mie theory.[26] The radii of the spheres were calculated as $R_S(x) = R_{p0}x^{1/3}$, while the scattered light intensity from the whole distribution has been computed as:

$$\langle I(q,t)\rangle = \frac{\int_0^\infty \omega(x,t)\, I(x,q,t)\, dx}{\int_0^\infty \omega(x,t)\, dx} \tag{29}$$

Note that $\langle I(q,t)\rangle$ was then normalized by multiplication with a constant value. In the experimental conditions considered, the polarization of the light was shown to have no significant effect on the obtained function (data not shown). In Figure 6 the comparison between the experimental and the simulated $\langle I(q,t)\rangle$ at 60, 90 and 120 min, is reported for the 30% MMA case for the three concentrations investigated, corresponding to $\phi = 1\times10^{-5}, 2\times10^{-5}, 3\times10^{-5}$.

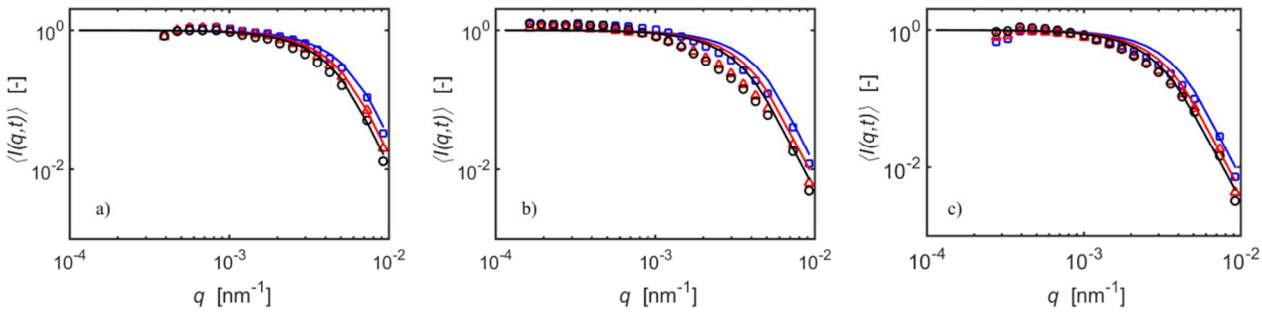

Figure 6 – Experimental (symbols) and predicted (continuous lines) $\langle I(q,t)\rangle$ at a) $\phi = 1\times10^{-5}$, b) $\phi = 2\times10^{-5}$ and c) $\phi = 3\times10^{-5}$ for three different times: 60 min (blue squares), 90 min (red triangles), and 120 min (black circles) for the 30% MMA particles. All the parameter values employed to obtain the model predictions are reported in Table D2 (ESI, Appendix D).

The reasonable accordance between experimental data and simulations indicates i) that the 30% MMA particles are significantly coalesced and ii) that such coalescence is not a complete one, as otherwise a full overlapping would have been observed.

The average fractal dimension of the clusters, $\langle d_f(t)\rangle$, was estimated from the experimental data at $t = 120\,\text{min}$ in order to provide a more direct glance at the aggregates spatial organization (cf. ESI, Appendix E, Table E1). Two different ways to calculate the $\langle d_f(t)\rangle$ have been used, namely taking the slope from the double log plot of $\langle S(q,t)\rangle$ *vs* q and from R_g *vs* I_0. In some cases it was not possible to employ the $\langle S(q,t)\rangle$ data in this sense, as the aggregates under investigation were too small to get a sufficiently large fractal regime. Notably, apart from the clusters made of 30% MMA particles, who significantly coalesce exhibiting a $\langle d_f(t)\rangle > 2.3$, all other systems have the typical $\langle d_f(t)\rangle$ of non-coalescing clusters in DLCA conditions. For the 60% and 70% MMA particles this is expected as their T_g is much

larger than the process temperature and therefore coalescence cannot occur. On the other hand, the 50% MMA containing particles showed a smaller $\langle R_g(t) \rangle$ (as compared to the 60% and 70% cases) and have a T_g which is slightly lower than the experimental temperature (17°C vs. 25°C), therefore an effect of coalescence on $\langle d_f(t) \rangle$ was expected to be present. This apparent contradiction can be understood by recalling the different characteristic times for the 50% MMA particles: $\tau_C \approx 4300s$, $\tau_A \approx 16-48s$ (according to the different ϕ, cf. Table 2) and $\tau_P \approx 9000s$. While $\tau_C >> \tau_A$ ($N >> 1$) and the initially formed clusters are indeed quite open and do not have the time to coalesce, the total process time is large enough ($\tau_P > \tau_C$) for the aggregates to undergo partial coalescence, i.e. case iii b). These aggregates are significantly ramified at their "birth" and their coalescence has to proceed through their branches first, before an extensive change in their structure is appreciated. Such process is particularly slow and therefore no evident change in the fractal dimension was appreciated. Interestingly, it turns out that while the $\langle d_f(t) \rangle$ is a useful tool to assess and quantify the extent of coalescence, in some cases measuring also the $\langle R_g(t) \rangle$ and $\langle R_h(t) \rangle$ is desirable as their time-evolution can be of great help in unravelling structural and spatial information about the aggregating-coalescing clusters.

5.3 Aggregation at higher temperatures

To further test the reliability of the developed model, experiments at higher temperatures (25-45°C) have been performed with the 60%, 50% and 30% MMA particles. The 70% MMA containing particles were not considered as their T_g is of about 55°C and these particles would therefore remain "rigid" even at 45°C; higher temperatures were not explored in order to avoid

water evaporation which could bias the experiments. Note that to properly compare the experimental results at different temperatures, the measured $\langle R_h(t)\rangle$ have been plotted against the non-dimensional time, τ_N :

$$\tau_N = \frac{t}{\tau_A} = t\beta_{11}C_{part} = t\frac{8}{3}\frac{k_B T}{\eta}C_{part} \tag{30}$$

Note that by employing τ_N, the effect of particle concentration and temperature are "filtered out", allowing to better appreciate the coalescence effect.

When considering the 30% MMA containing particles, it is worth mentioning that a significant coalescence was already observed at 25°C, being their T_g equal to -12°C. When increasing the temperature by 10 degrees, the situation was found to be almost unchanged, as shown in Figure F1 (Appendix F, ESI), where the $\langle R_h(t)\rangle$ of the 30% MMA particles is reported for both 25°C and 35°C against the non-dimensional time, τ_N.This means that a substantial coalescence (very likely an almost complete one) occurred in both cases and that for this reason no significant difference in $\langle R_h(t)\rangle$ can be appreciated; in fact in both cases $\tau_C \approx 100s$ was employed as fitting parameter.

When studying the 50% MMA containing particles (with a T_g of 17°C), a larger coalescence extent is expected when increasing the temperature above 25°C. Indeed, this is observed when measuring the $\langle R_h(t)\rangle$ vs. τ_N at 30°C, 35°C and 45°C: progressively smaller radii and radii increase are observed (cf. Figure 7).

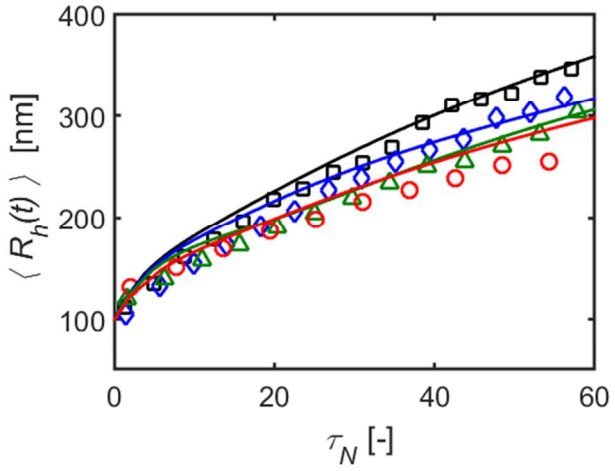

Figure 7 $\langle R_h(t) \rangle$ vs. time of the 50% MMA particles at 25°C (black squares), 30°C (blue diamonds), 35°C (green triangles) and 45°C (red circles) along with the corresponding simulations (continuous lines). All the parameter values employed to obtain the model predictions are reported in Table D3 (ESI, Appendix D).

Increasing the temperature, the softness of the particles increases, causing the clusters to be more compact and slower aggregating, an effect already discussed in the frame of the composition change for the $\langle R_g(t) \rangle$ and $\langle R_h(t) \rangle$ data set at lower temperature. When fitting τ_C against the experimental $\langle R_h(t) \rangle$ data, the following results are obtained: 1100s, 360s, and 210s, for 30°C, 35°C and 45°C, respectively. The simulation results are reported in Figure 7 (continuous lines). Once more the quality of the prediction is quite good, considering that only one fitting parameter, τ_C, has been used. Given the optimized values, it is possible to compare them to τ_A (cf. Table 2) in the frame of the four limiting cases identified in paragraph 5.1. At 25°C $\tau_C > \tau_A$ and partial coalescence occurs because of the long process times, cf. case iii b). When the temperature is raised, τ_C progressively decreases almost approaching a situation where $\tau_C \approx \tau_A$.

As a result, the coalescence extent is expected to be larger (indeed the radii are smaller) and the aggregation kinetics slowed down due to the diminished collision radii. Note that, beyond 35°C the coalescence seems to be almost complete as little difference is observed between the experimental $\langle R_h(t) \rangle$ at 35°C and 45°C. The model slightly overestimates such predictions of almost fully coalesced systems, as already seen at lower temperatures with the 30% MMA particles. When plotting the fitted τ_C of the 50% MMA case against 1/T in a semilog plot (cf. Figure F2, Appendix F, ESI), it is possible to appreciate the temperature dependency, already observed in the literature for both metallic and polymeric particles:[10, 14]

$$\tau_C = A \exp\left(\frac{B}{T}\right) \tag{31}$$

A similar analysis (at T = 25, 30, 35, and 45°C) was conducted with the 60% MMA containing particles but for the sake of brevity it has not been shown. Moreover, as the 60% MMA particles possess a T_g of about 35°C, no real difference between the samples is observed between 25°C and 30°C. Even beyond this temperatures (i.e. for 35°C and 45°C) only mild differences have been observed experimentally.

6 Conclusions

In the present paper, a deterministic model accounting for the simultaneous aggregation and coalescence of colloidal particles has been developed. The model is based on 1-D population balance equations (PBE), whose solution gives access to the particle size distribution as a function of time. The occurring coalescence is accounted for employing one parameter, the characteristic time of coalescence, τ_C. Literature correlations,[22] linking the PBE to experimental

light-scattering information such as $\langle R_h(t)\rangle$, $\langle R_g(t)\rangle$ and $\langle S_q(t)\rangle$, have been extended in order to account for partial coalescence.

The developed model has then been successfully tested against light scattering data of DLCA aggregating colloidal particles. In particular, by tuning the available parameter τ_C, it was possible to well-reproduce the observed experimental trends employing polymeric particles exhibiting a broad range of glass transition temperature values (-12°C - 55°C) in a range of temperatures comprised between 25°C and 45°C. Limitations of the model were found when the coalescence extent was significant, whereas for partial and no coalescence a good accordance was observed, both in terms of average sizes $\langle R_g(t)\rangle$ and $\langle R_h(t)\rangle$, as well as for structural parameters, such as $\langle S_q(t)\rangle$ and $\langle d_f(t)\rangle$.

Based on the characteristic times of aggregation (τ_A), coalescence (τ_C) and the entire aggregation process (τ_P), it was possible to identify three limiting cases, useful to appreciate the extent of coalescence and the resulting cluster spatial organization. Recalling that $\tau_P > \tau_A$ in all cases, as otherwise no aggregation would take place, and introducing the ratio of characteristic time of doublet coalescence over aggregation, $N = \tau_C / \tau_A$, it is possible to distinguish among the following situations. i) full, instantaneous coalescence occurs when $N << 1$ and uniform, compact clusters are obtained all along the aggregation process; ii) doublet aggregation and coalescence are occurring at a comparable rate for $N \approx 1$. Since $\tau_P > \tau_A \approx \tau_C$ rather uniform, compact aggregates are formed as the clusters coalesce while growing; iii a) no coalescence occurs and open clusters are formed when $N >> 1$ and $\tau_P < \tau_C$; iii b) coalescence occurs slowly and only after the clusters are formed when $N >> 1$ and $\tau_P > \tau_C$. The initially formed clusters

will be rather open; while for large enough τ_P, the aggregates branches will start to coalesce, hence the cluster "history" becomes of significant importance. For $\tau_P \to \infty$ the clusters will fully coalesce and become comparable to the situation of case i).

This analysis revealed, among other things, how the fractal dimension of the clusters is not always enough to appreciate partial coalescence (cf. case iii b)) and that by measuring $\langle R_g(t) \rangle$ and $\langle R_h(t) \rangle$ a more complete picture is obtained.

The present model might be of help in better characterizing and controlling colloidal processes where the interplay of aggregation and coalescence regulates the clusters size and structure, which is of great practical importance for the final applications.

Acknowledgements

S.L. gratefully acknowledges the Swiss National Science Foundation (SNSF) for financial support (grant number P2EZP2_159128). M.L. also gratefully acknowledges SNSF for financial support (grant number PP00P2133597/1).

References

1. Cosgrove, T. *Colloid science principles, methods and applications*; 2nd ed.; Wiley: Chichester, U.K., 2010. p 375 S.
2. Berg, J. C. *An introduction to interfaces & colloids - the bridge to nanoscience*; World Scientific: Hackensack, 2010. p 785.
3. Lin, M. Y.; Lindsay, H. M.; Weitz, D. A.; Ball, R. C.; Klein, R.; Meakin, P. Universality in Colloid Aggregation. *Nature* **1989,** *339* (6223), 360-362.
4. Ulrich, G. D.; Subramanian, N. S. Particle Growth in Flames .3. Coalescence as a Rate-Controlling Process. *Combust Sci Technol* **1977,** *17* (3-4), 119-126.
5. Koch, W.; Friedlander, S. K. The Effect of Particle Coalescence on the Surface-Area of a Coagulating Aerosol. *J Colloid Interf Sci* **1990,** *140* (2), 419-427.
6. von Smoluchowski, M. Experiments on a mathematical theory of kinetic coagulation of coloid solutions. *Z Phys Chem-Stoch Ve* **1917,** *92* (2), 129-168.

7. Xiong, Y.; Akhtar, M. K.; Pratsinis, S. E. Formation of Agglomerate Particles by Coagulation and Sintering .2. The Evolution of the Morphology of Aerosol-Made Titania, Silica and Silica-Doped Titania Powders. *J Aerosol Sci* **1993,** *24* (3), 301-313.
8. Xiong, Y.; Pratsinis, S. E. Formation of Agglomerate Particles by Coagulation and Sintering .1. A 2-Dimensional Solution of the Population Balance Equation. *J Aerosol Sci* **1993,** *24* (3), 283-300.
9. Buesser, B.; Grohn, A. J.; Pratsinis, S. E. Sintering Rate and Mechanism of TiO2 Nanoparticles by Molecular Dynamics. *J Phys Chem C* **2011,** *115* (22), 11030-11035.
10. Tsantilis, S.; Briesen, H.; Pratsinis, S. E. Sintering time for silica particle growth. *Aerosol Sci Tech* **2001,** *34* (3), 237-246.
11. Gauer, C.; Wu, H.; Morbidelli, M. Control of Coalescence in Clusters of Elastomer Colloids through Manipulation of Polymer Composition. *Macromolecules* **2009,** *42* (22), 9103-9110.
12. Gauer, C.; Wu, H.; Morbidelli, M. Effect of Surface Properties of Elastomer Colloids on Their Coalescence and Aggregation Kinetics. *Langmuir* **2009,** *25* (20), 12073-12083.
13. Gauer, C.; Jia, Z. C.; Wu, H.; Morbidelli, M. Aggregation Kinetics of Coalescing Polymer Colloids. *Langmuir* **2009,** *25* (17), 9703-9713.
14. Jia, Z. C.; Wu, H.; Morbidelli, M. Thermal restructuring of fractal clusters: The case of a strawberry-like core-shell polymer colloid. *Langmuir* **2007,** *23* (10), 5713-5721.
15. Gauer, C.; Wu, H.; Morbidelli, M. Reduction of Surface Charges during Coalescence of Elastomer Particles. *J Phys Chem B* **2010,** *114* (27), 8838-8845.
16. Sajjadi, S. Particle formation under monomer-starved conditions in the semibatch emulsion polymerisation of styrene. Part II. Mathematical modelling. *Polymer* **2003,** *44* (1), 223-237.
17. Harshe, Y. M.; Lattuada, M.; Soos, M. Experimental and Modeling Study of Breakage and Restructuring of Open and Dense Colloidal Aggregates. *Langmuir* **2011,** *27* (10), 5739-5752.
18. Kryven, I.; Lazzari, S.; Storti, G. Population Balance Modeling of Aggregation and Coalescence in Colloidal Systems. *Macromol Theor Simul* **2014,** *23* (3), 170-181.
19. Kostoglou, M.; Konstandopoulos, A. G. Evolution of aggregate size and fractal dimension during Brownian coagulation. *J Aerosol Sci* **2001,** *32* (12), 1399-1420.
20. Kryven, I.; Iedema, P. D. A Novel Approach to Population Balance Modeling of Reactive Polymer Modification Leading to Branching. *Macromol Theor Simul* **2013,** *22* (2), 89-106.
21. Eggersdorfer, M. L.; Kadau, D.; Herrmann, H. J.; Pratsinis, S. E. Multiparticle Sintering Dynamics: From Fractal-Like Aggregates to Compact Structures. *Langmuir* **2011,** *27* (10), 6358-6367.
22. Lattuada, M.; Wu, H.; Morbidelli, M. Hydrodynamic radius of fractal clusters. *J Colloid Interf Sci* **2003,** *268* (1), 96-105.
23. Lattuada, M.; Wu, H.; Morbidelli, M. A simple model for the structure of fractal aggregates. *J Colloid Interf Sci* **2003,** *268* (1), 106-120.
24. Nicoud, L.; Lazzari, S.; Barragan, D. B.; Morbidelli, M. Fragmentation of Amyloid Fibrils Occurs in Preferential Positions Depending on the Environmental Conditions. *J Phys Chem B* **2015,** *119* (13), 4644-4652.
25. Kestin, J.; Khalifa, H. E.; Correia, R. J. Tables of the Dynamic and Kinematic Viscosity of Aqueous Kci Solutions in the Temperature-Range 25-150-Degrees-C and the Pressure Range 0.1-35 Mpa. *J Phys Chem Ref Data* **1981,** *10* (1), 57-70.
26. Bohren, C. F.; Huffman, D. R. *Absorption and scattering of light by small particles*; Wiley-VCH Verlag: Weinheim, 2015. p 700 S.